7. 三宅病研究に残された謎

優性遺伝型の三宅病に*RP1L1*の変異が関与していることが明らかになったが，同時に新たな疑問点も生じている．*RP1L1*は霊長類の錐体視細胞だけでなく杆体視細胞にも発現しているが，三宅病で視細胞機能が低下するのは黄斑部に限られている．スペクトラルドメインOCTで三宅病の視細胞層を観察すると，発症から30年以上経過しても黄斑部以外の視細胞構造が正常に保たれている例が多い．なぜ，長期間経過しても杆体の機能が低下しないのか，黄斑部以外の錐体が障害を受けないのか．また，視細胞が変性，萎縮に陥っているにもかかわらず，なぜ網膜色素上皮は最後まで正常に保たれるのか．これらは錐体・杆体ジストロフィーなど，他の網膜疾患では一般にみられない所見である．

これらの疑問を解決するためには，ヒトにおける*RP1L1*発現の正確な局在を明らかにするだけでなく，遺伝子変異から視細胞の構造異常および機能異常に至るまでの詳細なメカニズムを今後の研究によって解明する必要がある．

お わ り に

三宅病の発見に至る経緯から疾患の特徴，診断法，あるいは今後の研究課題についてまとめた．

■文　献

1) 小口忠太：一種の夜盲症について．日眼会誌 **11**: 123-130, 1907.

2) Dryja TP, et al: A point mutation of the rhodopsin gene in one form of retinitis pigmentosa. Nature **343**(6256): 364-366, 1990.

3) Fuchs S, et al: A homozygous 1-base pair deletion in the arrestin gene is a frequent cause of Oguchi disease in Japanese. Nat Genet **10**(3): 360-362, 1995.

4) Miyake Y, et al: Hereditary macular dystrophy without visible fundus abnormality. Am J Ophthalmol **108**: 292-299, 1989.

5) Miyake Y, et al: Occult macular dystrophy. Am J Ophthalmol **122**: 644-653, 1996.

6) Akahori M, et al: Dominant mutations in *RP1L1* are responsible for occult macular dystrophy. Am J Hum Genet **87**: 424-429, 2010.

7) Miyake Y: Electrodiagnosis of Retinal Diseases, Springer-Verlag, Tokyo, 2006.

8) 藤波　芳，角田和繁：黄斑ジストロフィの遺伝子異常．眼科 **53**: 239-255, 2011.

9) Hirose T, et al: Simultaneous recording of electroretinogram and visual evoked response. Focal stimulation under direct observation. Arch Ophthalmol **95**(7): 1205-1208, 1977.

10) Arden GB, Bankes JL: Foveal electroretinogram as a clinical test. Br J Ophthalmol **50**(12): 740, 1966.

11) 三宅養三：黄斑部局所ERGでなにが分かる？　臨眼 **56**: 680-688, 2002.

12) Miyake Y, Awaya S: Stimulus deprivation amblyopia. Simultaneous recording of local macular electroretinogram and visual evoked response. Arch Ophthalmol **102**(7): 998-1003, 1984.

13) Miyake Y, et al: Local macular electroretinographic responses in idiopathic central serous chorioretinopathy. Am J Ophthalmol **106**(5): 546-550, 1988.

14) Miyake Y, et al: Oscillatory potentials in electroretinograms of the human macular region. Invest Ophthalmol Vis Sci **29**(11): 1631-1635, 1988.

15) Miyake Y, et al: Asymmetry of focal ERG in human macular region. Invest Ophthalmol Vis Sci **30**(8): 1743-1749, 1989.

16) Miyake Y, et al: Focal macular electroretinogram in X-linked congenital retinoschisis. Invest Ophthalmol Vis Sci **34**(3): 512-515, 1993.

17) Sutter EE, Tran D: The field topography of ERG components in man―I. The photopic luminance

response. Vision Res **32**: 433-446, 1992.

18) Piao CH, et al: Multifocal electroretinogram in occult macular dystrophy. Invest Ophthalmol Vis Sci **41**: 513-517, 2000.

19) Nakamura M, et al: A case of occult macular dystrophy accompanying normal tension glaucoma. Am J Ophthalmol **135**: 715-717, 2003.

20) Kondo M, et al: Foveal thickness in occult macular dystrophy. Am J Ophthalmol **135**: 725-728, 2003.

21) Wildberger H, et al: Multifocal electroretinogram(mfERG) in a family with occult macular dystrophy (OMD). Klin Monatsbl Augenheilkd **220**: 111-115, 2003.

22) Lyons JS: Non-familial occult macular dystrophy. Doc Ophthalmol **111**: 49-56, 2005.

23) Brockhurst RJ, Sandberg MA: Optical coherence tomography findings in occult macular dystrophy. Am J Ophthalmol **143**: 516-518, 2007.

24) Lubinski W, et al: A 43-year-old man with reduced visual acuity and normal fundus: occult macular dystrophy—case report. Doc Ophthalmol **116**: 111-118, 2008.

25) Fujinami K, et al: Fundus autofluorescence in autosomal dominant occult macular dystrophy. Arch Ophthalmol **129**: 597-602, 2011.

26) Park SJ, et al: Morphologic photoreceptor abnormality in occult macular dystrophy on spectral-domain optical coherence tomography. Invest Ophthalmol Vis Sci **51**: 3673-3679, 2010.

27) Hanazono G, et al: Pattern-reversal visual-evoked potential in patients with occult macular dystrophy. Clin Ophthalmol **4**: 1515-1520, 2010.

28) Tsunoda K, et al: Clinical characteristics of occult macular dystrophy in family with mutation of RP1l1 gene. Retina **32**(6): 1135-1147, 2012.

29) Conte I, et al: Identification and characterisation of the retinitis pigmentosa 1-like 1 gene(*RP1L1*): a novel candidate for retinal degenerations. Eur J Hum Genet **11**: 155-162, 2003.

30) Yamashita T, et al: Essential and synergistic roles of RP1 and *RP1L1* in rod photoreceptor axoneme and retinitis pigmentosa. J Neurosci **29**: 9748-9760, 2009.

Outer Retinal Morphology and Visual Function in Patients With Idiopathic Epiretinal Membrane

Ken Watanabe, MD; Kazushige Tsunoda, MD, PhD; Yoshinobu Mizuno, MD; Kunihiko Akiyama, MD; Toru Noda, MD

Objective: To determine the relationship between the morphology of the fovea and visual acuity in patients with an untreated idiopathic epiretinal membrane (ERM).

Methods: We examined 52 eyes of 45 patients diagnosed with an ERM. The morphology of the foveal area was determined by spectral-domain optical coherence tomography. The relationships between the best-corrected visual acuity (BCVA) and 8 optical coherence tomography features, central retinal thickness, cone outer segment tip (COST) line, photoreceptor inner/outer segment (IS/OS) junction line, foveal bulge of the IS/OS line, external limiting membrane, inner limiting membrane, foveal pit, and ERM over the foveal center, were evaluated.

Results: Multiple regression analysis showed that intact COST line, IS/OS junction line, and external limiting membrane independently and significantly contrib-

uted to the BCVA. The standardized partial regression coefficient β was 0.415 for the COST line, 0.287 for the IS/OS junction line, and 0.247 for the external limiting membrane. However, the other features, eg, foveal bulge, inner limiting membrane, foveal pit, and ERM, were not significantly associated with the BCVA. The central retinal thickness was significantly correlated with the BCVA ($r^2 = 0.274$; $P < .01$).

Conclusions: At an early stage of an ERM, only the photoreceptor structures are significantly associated with the BCVA, and the appearance of the COST line was most highly associated. Detailed examinations of the photoreceptor structures using optical coherence tomography may help find photoreceptor dysfunction in cases of idiopathic ERM.

JAMA Ophthalmol. 2013;131(2):172-177
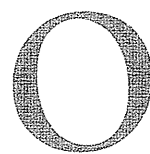
O PTICAL COHERENCE TO-mography (OCT) is a useful method of detecting early morphological changes in retinas affected by various pathological conditions. The correlations between the visual acuity and the morphological changes in the retina have been reported for various retinal diseases, such as age-related macular degeneration,[1] central serous chorioretinopathy,[2] macular edema,[3,4] idiopathic macular hole,[5,6] and epiretinal membrane (ERM).[7-9]

Retinal traction caused by an ERM leads to morphological changes of not only the superficial layers of the retina but also the entire retina including the photoreceptor layer. This is important because long-standing morphological changes can lead to functional damages and cause metamorphopsia and decreased visual acuity.

Spectral-domain OCT (SD-OCT) has enabled clinicians and investigators to obtain clearer images of the microstructure of the photoreceptor layer than time-domain OCT. Several studies have examined whether significant correlations exist between macular dysfunction and the integrity of photoreceptor microstructures, especially the photoreceptor inner

segment/outer segment (IS/OS) junction line, detected by SD-OCT in patients with an ERM.[7-10]

The diagnostic value of determining the integrity of the IS/OS junction line and the cone outer segment tip (COST) line by SD-OCT has been done primarily on diseases of the outer retina, eg, acute zonal occult outer retinopathy[11] and hereditary macular dystrophies.[12-14] However, in eyes with an ERM, the appearance of the photoreceptor microstructures in the SD-OCT image can be affected by retinal thickening, subretinal cysts, and the ERM itself. These alterations lead to a reduction in the intensity of the laser light reaching the photoreceptor layer. In addition, the clarity of the SD-OCT images of the outer retina, eg, the Henle layer, IS/OS junction line, and COST line, is dependent on the incidence angle of the laser beam on the retina, which would be altered by an ERM.[15,16] Thus, the diagnostic value of examining the photoreceptor microstructures by SD-OCT in eyes with an ERM may not be as reliable as in cases of acute zonal occult outer retinopathy and other outer retinal diseases where the inner retinal alterations do not attenuate the laser energy.

The purpose of this study was to evaluate the relationship between deteriora-

Author Affiliations: Department of Ophthalmology, National Tokyo Medical Center (Drs Watanabe, Akiyama, and Noda), and Laboratory of Visual Physiology, National Institute of Sensory Organs (Drs Tsunoda and Mizuno), Tokyo, Japan.

tion of the best-corrected visual acuity (BCVA) and abnormalities of the photoreceptor microstructures in patients with untreated idiopathic ERM. To accomplish this, we examined cases with ERM without severely deformed inner structures, such as a lamellar hole and large cystic formations. We classified the abnormalities of the retina in the SD-OCT images and performed multiple regression analyses to determine which parameter was independently and significantly associated with the BCVA in cases of ERM.

METHODS

This was a retrospective case series performed in the Department of Ophthalmology, National Tokyo Medical Center, Tokyo, Japan. After an explanation of the procedures to be used, an informed consent was received from all of the subjects for the tests. The procedures used adhered to the tenets of the Declaration of Helsinki, and approval to perform this study was obtained from the review board/ethics committee of the Tokyo Medical Center.

We examined 52 eyes of 45 patients (20 eyes of 18 men and 32 eyes of 27 women, mean [SD] age, 67.0 [10.0] years) diagnosed with an ERM without lamellar holes or apparent cystic changes in the fovea. The patients were examined between October 2009 and September 2010. The exclusion criteria were myopia more than 6 diopters, advanced lens opacification, other ocular disease that could cause visual disturbances, secondary ERM caused by vascular diseases, uveitis, and retinal detachment. Cases whose OCT images did not have enough signal intensity for evaluation, ie, average intensity of the SD-OCT signal was less than 8 of 10, were also excluded.

Spectral-domain OCT (Cirrus HD-OCT, versions 4.5 and 5.1; Carl Zeiss Meditec) was used to obtain tomographic images of the retina. Following dilation of the pupil, 5 line-scan images were obtained both horizontally (length, 9.0 mm) and vertically (length, 6.0 mm) across the foveola, with the distance between each scan line of 0.075 mm. Cases where any of the scan lines did not pass through the foveola were excluded.

Eight SD-OCT features were evaluated: (1) central retinal thickness (CRT), (2) COST line, (3) IS/OS junction line, (4) bulgelike appearance of the IS/OS junction line at the foveola (foveal bulge), (5) external limiting membrane (ELM), (6) internal limiting membrane (ILM), (7) foveal pit, and (8) ERM formation over the foveal center.

The CRT was defined as the distance between the inner retinal surface and inner surface of the retinal pigment epithelium at the foveola (Figure 1A). It was measured manually by the built-in scale of the SD-OCT system.

The microstructures within a 500-μm diameter of the fovea (Figure 1A, scale bar) were graded independently by 2 experienced ophthalmologists (K.W. and K.T.) (Table 1) to be either normal or abnormal. During this procedure, all the patients' information, including the BCVA, was masked to the examiners. In cases where the gradings were different, discussions were held until both examiners agreed. In earlier studies, the OCT features were graded into 3 classes, eg, normal ILM, mild ILM distortion, and severe ILM distortion.[7,9,17] We initially adopted a similar classification; however, we found it confusing especially in distinguishing mildly from severely abnormal structures. We have thus simplified the classification to normal or abnormal.

The COST line, IS/OS junction line, and ELM were graded normal when they were seen clearly and appeared continuous in the foveal region, and they were graded abnormal when they were blurred, interrupted, or absent. The foveal bulge is an elevation of the IS/OS junction line that appears like a dome over

the foveola. We graded it normal when the bulgelike appearance was clearly observed and graded it abnormal when the bulgelike appearance was not observed and the IS/OS junction line appeared flat.

The ILM was graded normal when it looked smooth and flat at the fovea and was graded abnormal when it looked wrinkled or distorted. The foveal pit was graded normal when the concave retinal surface was clearly observed at the foveola and graded abnormal when the foveal surface appeared flat. The ERM was graded normal when the ERM did not overlap the foveola and graded abnormal when the ERM was attached over the foveola.

The relationship between these 8 OCT features and the visual acuity was statistically examined. Statistical analysis was performed using SPSS version 19.0 (SPSS Japan). The visual acuity was converted to logMAR units for the statistical analyses. Pearson correlations were performed to determine the association between CRT and visual acuity. The Mann-Whitney test was used to compare the BCVA and CRT between the normal and abnormal groups for each OCT feature. Multiple regression analysis was performed with BCVA and CRT as the dependent variables and with the integrities of 7 OCT features as independent variables. A P value <.05 was considered significant.

RESULTS

We first evaluated the normal fellow eyes of 29 of the 45 patients studied (13 eyes of 13 men and 16 eyes of 16 women; mean [SD] age, 66.0 [8.1] years). For these, all of the 7 OCT features were judged normal.[18]

Two representative cases demonstrating how the OCT features were judged to be either normal or abnormal are shown in Figure 1B and C. A horizontal SD-OCT scan image of the left retina of a 74-year-old man is shown in Figure 1B. The ELM, foveal bulge, IS/OS junction line, and COST line were clearly observed and judged to be normal. An ERM was present over the foveola, and this was judged to be abnormal. The foveal pit was concave and judged to be normal. The ILM was partially wrinkled at the foveola and judged abnormal.

A vertical SD-OCT scan image of the right retina of a 65-year-old woman is shown in Figure 1C. The IS/OS junction line and ELM were clearly observed and judged to be normal. The foveal bulge and COST line could not be seen at the fovea and were judged abnormal. The ILM was wrinkled in the parafoveal region; however, the foveal region within 500 μm of the foveola was spared and judged normal. The foveal pit was judged abnormal because the fovea was elevated by a tangential traction from the ERM and the foveal pit was flattened. An ERM covered the foveola and was judged abnormal.

The BCVA and CRT of the normal eyes were compared with those of the abnormal groups for each OCT feature of the 52 cases by Mann-Whitney test (Figure 2). The BCVA was significantly better in cases when 6 OCT features were judged to be normal: COST line, IS/OS junction line, foveal bulge, ELM, foveal pit, and ERM (Figure 2A). The CRT was significantly thinner in cases when 5 OCT features were judged to be normal: COST line, IS/OS junction line, foveal bulge, foveal pit, and ERM (Figure 2B).

Subsequently, multiple regression analyses were performed to determine the independent predictors of the BCVA and CRT in eyes with an ERM. The analyses showed
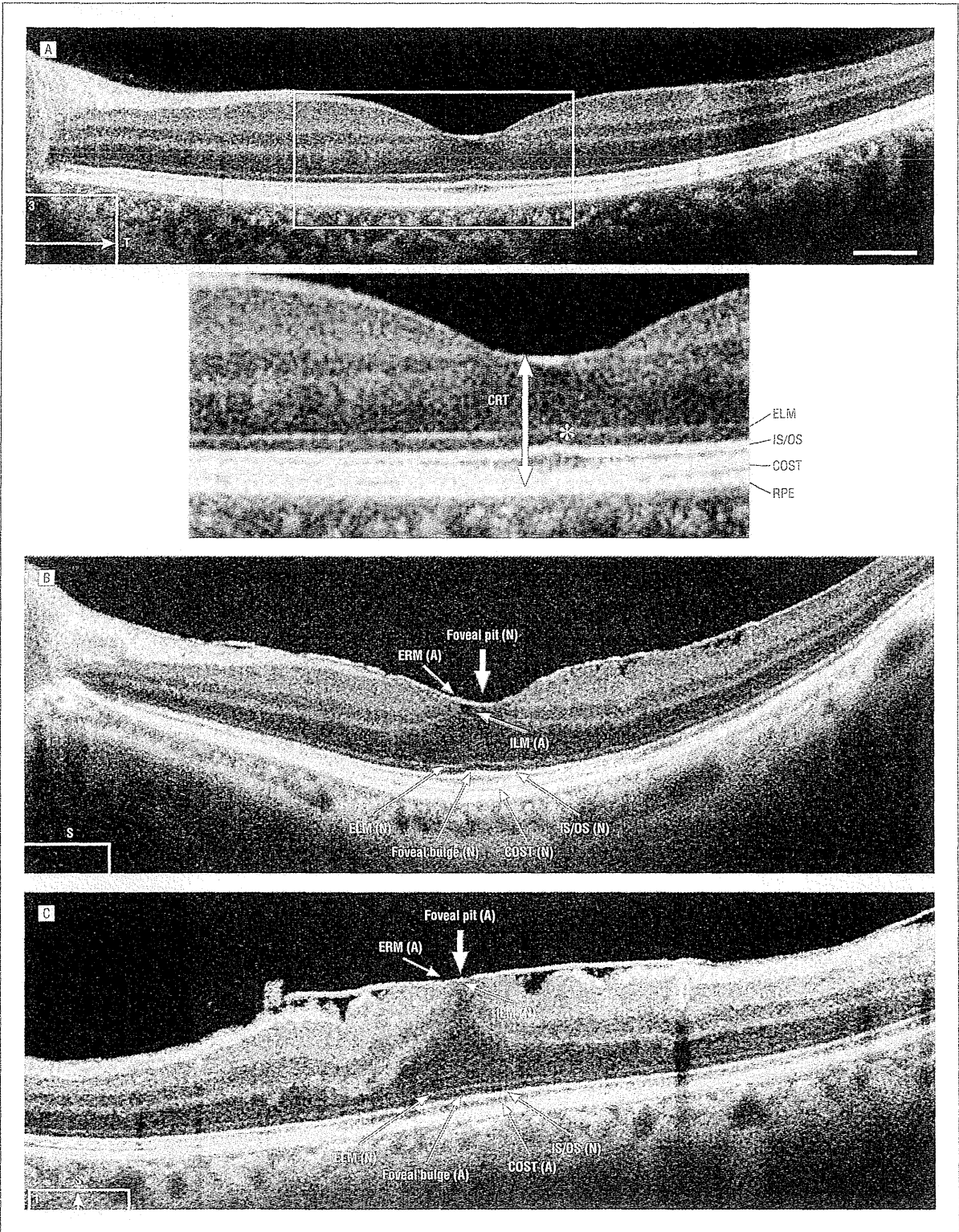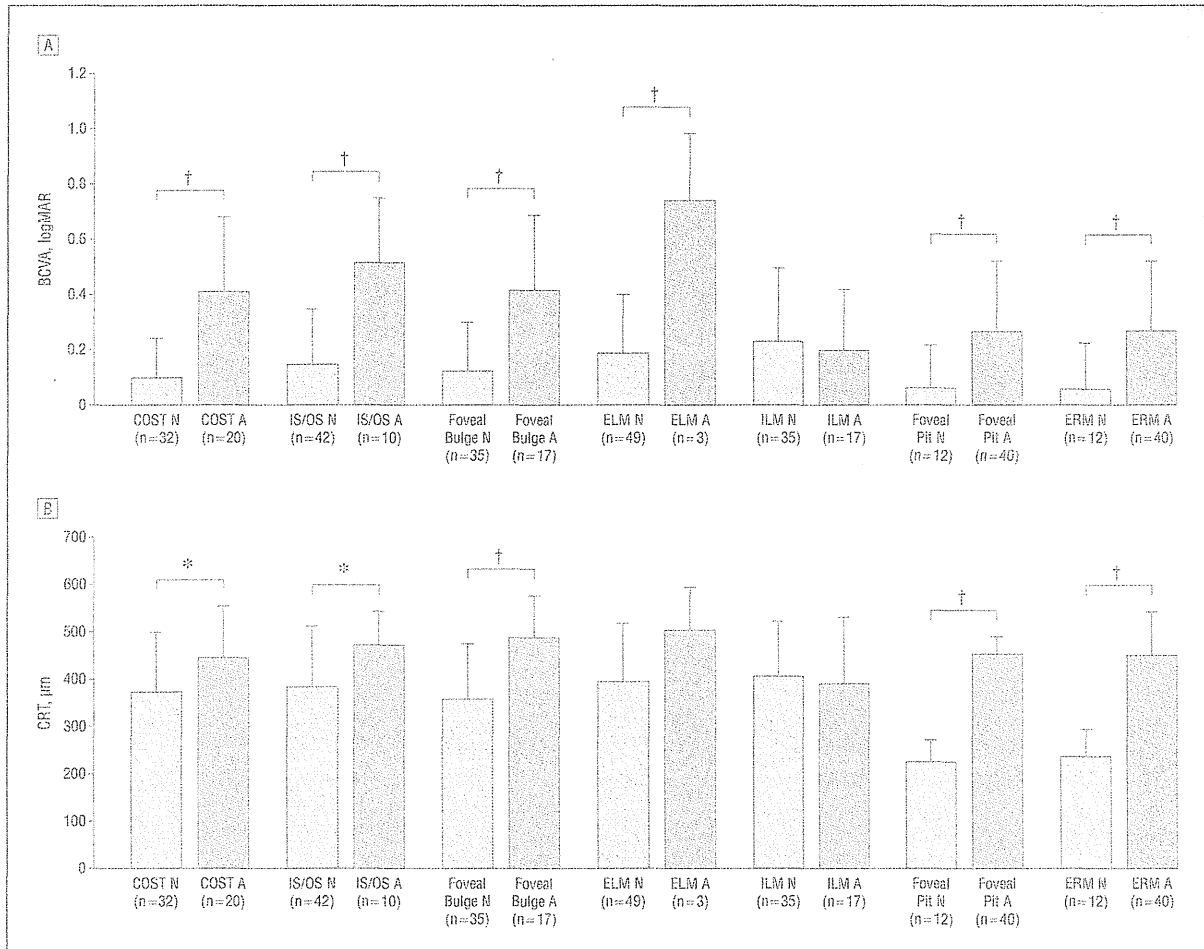
Figure 1. Optical coherence tomography images. A, Horizontal optical coherence tomography image of the retina of a normal eye with a magnified image showing the locations of the external limiting membrane (ELM), photoreceptor inner segment/outer segment junction line (IS/OS), cone outer segment tip line (COST), retinal pigment epithelium (RPE), foveal bulge (asterisk), and central retinal thickness (CRT) (arrow). Scale bar=500 μm. B and C, Classification of 7 features in spectral-domain optical coherence tomography image in patients with an epiretinal membrane (ERM). A indicates abnormal; ILM, internal limiting membrane; and N, normal.

Table 1. Classification of OCT Features in the Foveal Region

Classification	COST	IS/OS	Foveal Bulge	ELM	ILM	Foveal Pit	ERM
Normal	Clear and continuous	Clear and continuous	Observed	Clear and continuous	Smooth and flat	Observed	Foveola is free of ERM
Abnormal	Blurred, interrupted, or absent	Blurred, interrupted, or absent	Not observed	Blurred, interrupted, or absent	Wrinkled or distorted	Not observed	ERM is attached over foveola

Abbreviations: COST, cone outer segment tip line; ELM, external limiting membrane; ERM, epiretinal membrane; ILM, internal limiting membrane; IS/OS, photoreceptor inner segment/outer segment junction line; OCT, optical coherence tomography.

Figure 2. Comparisons between normal (N) and abnormal (A) eyes for 7 optical coherence tomography features. A, Best-corrected visual acuity (BCVA). B, Central retinal thickness (CRT). Mann-Whitney test, *$P < .05$ and †$P < .01$. COST indicates cone outer segment tip line; ELM, external limiting membrane; ERM, epiretinal membrane; ILM, internal limiting membrane; and IS/OS, inner segment/outer segment junction line.

that the predictive variables for BCVA were COST line ($P < .001$), IS/OS junction line ($P = .02$), and ELM ($P = .03$). The standardized partial regression coefficient β was 0.415 for the COST line, 0.287 for the IS/OS junction line, and 0.247 for the ELM (Table 2). On the other hand, the predictive variables for the CRT were foveal pit ($P < .001$), ERM ($P = .003$), and foveal bulge ($P = .04$). The standardized partial regression coefficient β was 0.476 for the foveal pit, 0.337 for the ERM, and 0.182 for the foveal bulge (Table 3).

The CRT was measured at the foveal center in 52 cases, and a significantly positive correlation was observed between the CRT and the BCVA ($r^2 = 0.274; P < .01$) (Figure 3).

COMMENT

The relationships between the outer retinal microstructures determined by SD-OCT and the BCVA have been reported previously for patients with ERM.[7-10] The de-

Table 2. Multiple Regression Analyses to Determine the Independent Predictors of the Best-Corrected Visual Acuity

	Standardized Partial Regression Coefficient (β)	P Value
COST	0.415	<.001
IS/OS	0.287	.02
ELM	0.247	.03

Abbreviations: COST, cone outer segment tip line; ELM, external limiting membrane; IS/OS, photoreceptor inner segment/outer segment junction line.

Table 3. Multiple Regression Analyses to Determine the Independent Predictors of the Central Retinal Thickness

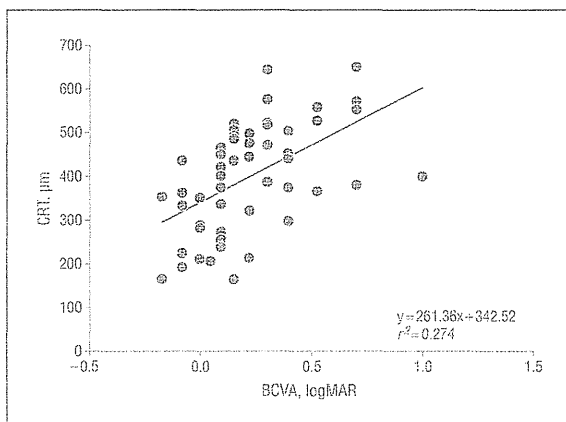|	Standardized Partial Regression Coefficient (β)	P Value
Foveal pit	0.476	<.001
ERM	0.337	.003
Foveal bulge	0.182	.04

Abbreviation: ERM, epiretinal membrane.

Figure 3. Significant correlation between central retinal thickness (CRT) and best-corrected visual acuity (BCVA) in 52 eyes. Pearson correlation coefficient r^2 was 0.274 ($P < .01$).

sign of our study was different from these earlier studies because we evaluated the OCT features only in the foveal region within 500 µm of the center because the visual acuity is mainly determined by the foveal center. In addition, we excluded patients who had small lamellar holes or apparent cystic changes in the fovea, which can induce optical artifacts and distort the appearances of the photoreceptor layer in the OCT images.

Multiple regression analyses showed that the integrity of the COST line was most strongly associated with the BCVA, followed by the IS/OS junction line and the ELM. On the other hand, the foveal bulge, ILM, foveal pit, and ERM were not significantly associated with the BCVA. It has been reported that the integrity of the IS/OS junction line is significantly associated with the postoperative BCVA.[7,8] Our results showed that not only the IS/OS junction but also the COST line were most strongly associated with the preoperative BCVA (β = 0.415 for

COST line; β = 0.287 for IS/OS junction). Abnormalities of the COST line have been suggested to be an early sign of photoreceptor dysfunction in eyes with outer retinal disorders.[11,19] In cases of ERM, the appearance of the COST line at the fovea should be carefully examined to determine if early changes in retinal function might be present.

In patients with an ERM, the retinal thickening could affect the appearance of the images of the photoreceptor layer. Multiple regression analysis showed that abnormalities in the COST line, IS/OS junction line, and ELM were not significantly associated with the CRT (Table 2 and Table 3), although an absence of the foveal pit ($P < .001$) and existence of foveal ERM over the foveola ($P = .003$) were independently associated with the CRT. These results suggest that the photoreceptor microstructures appeared abnormal not because of the reduced laser light through thickened retina but because of real morphological changes. The abnormality in the inner retinal structures, eg, ILM, foveal pit, and ERM at the foveola, might affect the visual acuity because they would alter the optical characteristics of the retina. However, the results of multiple regression analysis showed that these inner retinal abnormalities did not significantly contribute to the BCVA at least in the early stage of ERM.

The correlations between the 4 highly refractive bands in the outer retina seen in the SD-OCT images and the retinal histologic features have been well investigated.[16,20,21] There has been an early consensus on the interpretation of the first and fourth bands in the outer retina, the innermost band representing the ELM and the outermost band representing the complex of the retinal pigment epithelium and Bruch membrane. The second band was initially thought to arise from the differences in the refractive index between the inner and outer segments of the photoreceptor and thus called the photoreceptor IS/OS junction line. However, Fernández et al[21] found it to represent the ellipsoids of the photoreceptor inner segment by ultra high-resolution OCT with adaptive optics. The third band has been found to represent the junction between the cone outer segment and the apical microvillae of the retinal pigment epithelium and is called the COST line.[16,21] The ellipsoids in the photoreceptor inner segments are rich in mitochondria and crucial for the metabolism of the photoreceptors. The cone outer segments contain the photopigment discs, which are also important for phototransduction. The strong contributions of the COST and IS/OS junction lines to the BCVA but not to the CRT suggest that both the microstructure and function of the photoreceptors were damaged by the ERM.

The OCT abnormalities in the photoreceptor microstructures have been reported to be significantly correlated with the loss of visual acuity and visual field in acute zonal occult outer retinopathy and retinal dystrophies where the photoreceptors are primarily affected.[11-14] On the other hand, the abnormal ERM develops on the surface of the retina without directly affecting the photoreceptor layer. The membrane can then cause tangential traction over the macula, followed by an inward traction toward the vitreous cavity at the foveal pit. Long-standing inward traction may cause formations of cysts in the outer nuclear layer

and microstructural changes in the photoreceptor.[7,8,22,23] Thus, the etiology of the OCT abnormalities of the photoreceptor layer observed in eyes with an ERM should be different from that of outer retinal diseases.

Niwa et al[24] measured focal macular electroretinograms (fmERGs) elicited by 15° stimuli in 37 patients with an ERM and concluded that the inner retinal layer was predominantly impaired initially and that the visual dysfunction in eyes with ERM may have resulted from macular edema. They also found that the correlation between the visual acuity and the degree of amplitude reduction of the a wave, b wave, and oscillatory potentials was not significant. However, they reported that the visual acuity largely depended on a very limited region of the fovea, and the stimulated region of 15° in the fmERG was too large to evaluate the relationship between the BCVA and fmERGs. In fact, there are patients with macular dystrophy who have both good visual acuity and extinguished fmERGs.[19] In such patients, the function of a very small region of the fovea is spared. In cases of ERM, an inward traction is especially strong in the foveola as shown in Figure 1B and C, and the outer nuclear layer within 500 μm of the foveola is thicker than in the parafoveal region. Thus, the results of fmERGs elicited by 15° stimuli did not necessarily exclude the fact that the photoreceptor function was primarily affected by the ERM. Considering that mechanical traction is extraordinarily severe in the foveola, the photoreceptor function may be primarily impaired even at the early stage of ERM, leading to the reduction of the BCVA.

There are reports that the reduction in the visual acuity in eyes with an ERM is due to retinal thickening,[9,10] and our results also indicated that the thickness of the outer retina, ie, combined thickness of outer nuclear layer and photoreceptor layer, was correlated with visual acuity (Figure 3). Together with the results of multiple regression analysis, functional damage of the photoreceptor due to long-standing inward traction was determined to be a strong contributor to the visual acuity reduction. Thus, detailed examinations of the photoreceptor microstructures in the OCT images may help find early visual dysfunction in cases of idiopathic ERM.

REFERENCES

1. Keane PA, Liakopoulos S, Chang KT, et al. Relationship between optical coherence tomography retinal parameters and visual acuity in neovascular age-related macular degeneration. Ophthalmology. 2008;115(12):2206-2214.
2. Piccolino FC, de la Longrais RR, Ravera G, et al. The foveal photoreceptor layer and visual acuity loss in central serous chorioretinopathy. Am J Ophthalmol. 2005;139(1):87-99.
3. Otani T, Yamaguchi Y, Kishi S. Correlation between visual acuity and foveal microstructural changes in diabetic macular edema. Retina. 2010;30(5):774-780.
4. Ota M, Tsujikawa A, Murakami T, et al. Foveal photoreceptor layer in eyes with persistent cystoid macular edema associated with branch retinal vein occlusion. Am J Ophthalmol. 2008;145(2):273-280.
5. Itoh Y, Inoue M, Rii T, Hiraoka T, Hirakata A. Significant correlation between visual acuity and recovery of foveal cone microstructures after macular hole surgery. Am J Ophthalmol. 2012;153(1):111-119, e1.
6. Wakabayashi T, Fujiwara M, Sakaguchi H, Kusaka S, Oshima Y. Foveal microstructure and visual acuity in surgically closed macular holes: spectral-domain optical coherence tomographic analysis. Ophthalmology. 2010;117(9):1815-1824.
7. Falkner-Radler CI, Glittenberg C, Hagen S, Benesch T, Binder S. Spectral-domain optical coherence tomography for monitoring epiretinal membrane surgery. Ophthalmology. 2010;117(4):798-805.
8. Suh MH, Seo JM, Park KH, Yu HG. Associations between macular findings by optical coherence tomography and visual outcomes after epiretinal membrane removal. Am J Ophthalmol. 2009;147(3):473-480, e3.
9. Michalewski J, Michalewska Z, Cisiecki S, Nawrocki J. Morphologically functional correlations of macular pathology connected with epiretinal membrane formation in spectral optical coherence tomography (SOCT). Graefes Arch Clin Exp Ophthalmol. 2007;245(11):1623-1631.
10. Arichika S, Hangai M, Yoshimura N. Correlation between thickening of the inner and outer retina and visual acuity in patients with epiretinal membrane. Retina. 2010;30(3):503-508.
11. Tsunoda K, Fujinami K, Miyake Y. Selective abnormality of cone outer segment tip line in acute zonal occult outer retinopathy as observed by spectral-domain optical coherence tomography. Arch Ophthalmol. 2011;129(8):1099-1101.
12. Sergouniotis PI, Holder GE, Robson AG, Michaelides M, Webster AR, Moore AT. High-resolution optical coherence tomography imaging in KCNV2 retinopathy. Br J Ophthalmol. 2012;96(2):213-217.
13. Genead MA, Fishman GA, Rha J, et al. Photoreceptor structure and function in patients with congenital achromatopsia. Invest Ophthalmol Vis Sci. 2011;52(10):7298-7308.
14. Hood DC, Zhang X, Ramachandran R, et al. The inner segment/outer segment border seen on optical coherence tomography is less intense in patients with diminished cone function. Invest Ophthalmol Vis Sci. 2011;52(13):9703-9709.
15. Lujan BJ, Roorda A, Knighton RW, Carroll J. Revealing Henle's fiber layer using spectral domain optical coherence tomography. Invest Ophthalmol Vis Sci. 2011;52(3):1486-1492.
16. Srinivasan VJ, Monson BK, Wojtkowski M, et al. Characterization of outer retinal morphology with high-speed, ultrahigh-resolution optical coherence tomography. Invest Ophthalmol Vis Sci. 2008;49(4):1571-1579.
17. Mitamura Y, Hirano K, Baba T, Yamamoto S. Correlation of visual recovery with presence of photoreceptor inner/outer segment junction in optical coherence images after epiretinal membrane surgery. Br J Ophthalmol. 2009;93(2):171-175.
18. Rii T, Itoh Y, Inoue M, Hirakata A. Foveal cone outer segment tips line and disruption artifacts in spectral-domain optical coherence tomographic images of normal eyes. Am J Ophthalmol. 2012;153(3):524-529, e1.
19. Tsunoda K, Usui T, Hatase T, et al. Clinical characteristics of occult macular dystrophy in family with mutation of RP1L1 gene. Retina. 2012;32(6):1135-1147.
20. Spaide RF, Curcio CA. Anatomical correlates to the bands seen in the outer retina by optical coherence tomography: literature review and model. Retina. 2011;31(8):1609-1619.
21. Fernández EJ, Hermann B, Povazay B, et al. Ultrahigh resolution optical coherence tomography and pancorrection for cellular imaging of the living human retina. Opt Express. 2008;16(15):11083-11094.
22. Wilkins JR, Puliafito CA, Hee MR, et al. Characterization of epiretinal membranes using optical coherence tomography. Ophthalmology. 1996;103(12):2142-2151.
23. Gaudric A. Macular cysts, holes and cavitations: 2006 Jules Gonin lecture of the Retina Research Foundation. Graefes Arch Clin Exp Ophthalmol. 2008;246(7):1071-1079.
24. Niwa T, Terasaki H, Kondo M, Piao CH, Suzuki T, Miyake Y. Function and morphology of macula before and after removal of idiopathic epiretinal membrane. Invest Ophthalmol Vis Sci. 2003;44(4):1652-1656.

Functional Topography of Rod and Cone Photoreceptors in Macaque Retina Determined by Retinal Densitometry

Gen Hanazono,[1,2] *Kazushige Tsunoda,*[1,2] *Yoko Kazato,*[1,2] *Wataru Suzuki,*[1,2,3] *and Manabu Tanifuji*[2]

PURPOSE. The purpose of this study is to determine the topography of bleaching in rods, middle/long-wavelength (M/L) and short-wavelength (S) cones in the macaque retina by using a modified retinal densitometry technique.

METHODS. A modified commercial digital fundus camera system was used to measure continuously the intensity of the light reflectance during bleaching with band pass lights in the ocular fundus of three adult Rhesus monkeys (Macaca mulatta) under general anesthesia. The topography of bleaching in rods, M/L-, and S-cones was obtained separately by considering the characteristic time course of the reflectance changes, depending on the wavelengths of light and retinal locations.

RESULTS. The distribution of M/L-cones response had a steep peak at the foveal center and was elongated horizontally. The distribution of rod responses was minimum at the foveal center and maximum along a circular region at the eccentricity of the optic disc. The distribution of S-cone responses was highest at the fovea and was excavated centrally. There was a circular region with the maximal responses at 0.38 to 1.0 degrees from the foveal center.

CONCLUSIONS. With the current imaging technique, not only the steep peak of the M/L-cone responses at the fovea, but the ring-shaped distribution of rod responses in the periphery and the central reduction of S-cone response could be determined with good resolution. *(Invest Ophthalmol Vis Sci.* 2012;53:2796–2803) DOI:10.1167/iovs.11-9252

The human visual system is a duplex system, consisting of a rod system for scotopic conditions and a cone system for photopic conditions. Three types of cones mediate color vision; long (L), middle (M), and short (S) wavelength-sensitive cones. The distribution of the photoreceptors has been well investigated on postmortem eyes of humans and macaques.[1-9] These studies reported the anatomical densities of the different types of photoreceptors, but the results did not necessarily reflect their functional properties. Psychophysical experiments also have been used to assess photoreceptor function.[10-15] However, the results reflect not only the retinal function, but the visual function from the photoreceptors to the visual cortex.

Approximately 50 years ago, the time course of the bleaching of photopigments was determined quantitatively by measuring the reflectance changes during bleaching and regeneration of the visual pigments in human retinas.[16-22] This method, retinal densitometry, was used to determine the in vivo kinetics of the photopigments of cones and rods quite accurately. The spatial distribution of the reflectance changes was determined later by examining images obtained by either a fundus camera or a scanning laser ophthalmoscope (SLO), that is, imaging fundus reflectometry.[23-33] With these techniques, the distribution of photoreceptors was mapped objectively and non-invasively as bleach-derived light reflectance changes in normal and diseased eyes. However, the responses of the different types of photoreceptors, especially rods and S-cones, could not be segregated accurately because the response time courses were not monitored accurately.

We developed a new retinal densitometry system that can measure the retinal reflectance changes continuously after bleaching with band pass lights in anesthetized rhesus monkeys. We found that the time course of the reflectance changes depended not only on the wavelength of light but on the retinal location. By using such characteristics, the topography of bleaching in rods, M/L-, and S-cones could be obtained separately. The circular region of the maximal rod responses and the reduction of S-cone responses in the center were determined functionally with good spatial resolution.

METHODS

The experiments were performed on three adult Rhesus monkeys (Macaca mulatta). Following an intramuscular injection of atropine sulfate (0.08 mg/kg), the monkeys were anesthetized with droperidol (0.25 mg/kg) and ketamine (5.0 mg/kg), and then paralyzed with vecuronium bromide (0.1 mg/ kg/ hour). To block pain, fentanyl citrate (0.83 µg/kg/h) was infused intravenously continuously throughout the experiments. The animals were ventilated artificially with a mixture of 70% N_2O, 30% O_2, and 1.0–1.5% of isoflurane. The electroencephalograms (EEGs), electrocardiograms (ECGs), expired CO_2, and rectal temperature were monitored continuously throughout the experiments. Before the recordings, the pupils were dilated fully with topical tropicamide (0.5%) and phenylephrine hydrochloride (0.5%). The experimental protocol was approved by the Experimental Animal Committee of the RIKEN Institute, and all experimental procedures were carried out in accordance with the guidelines of the RIKEN Institute and the ARVO Statement for the Use of Animals in Ophthalmic and Vision Research.
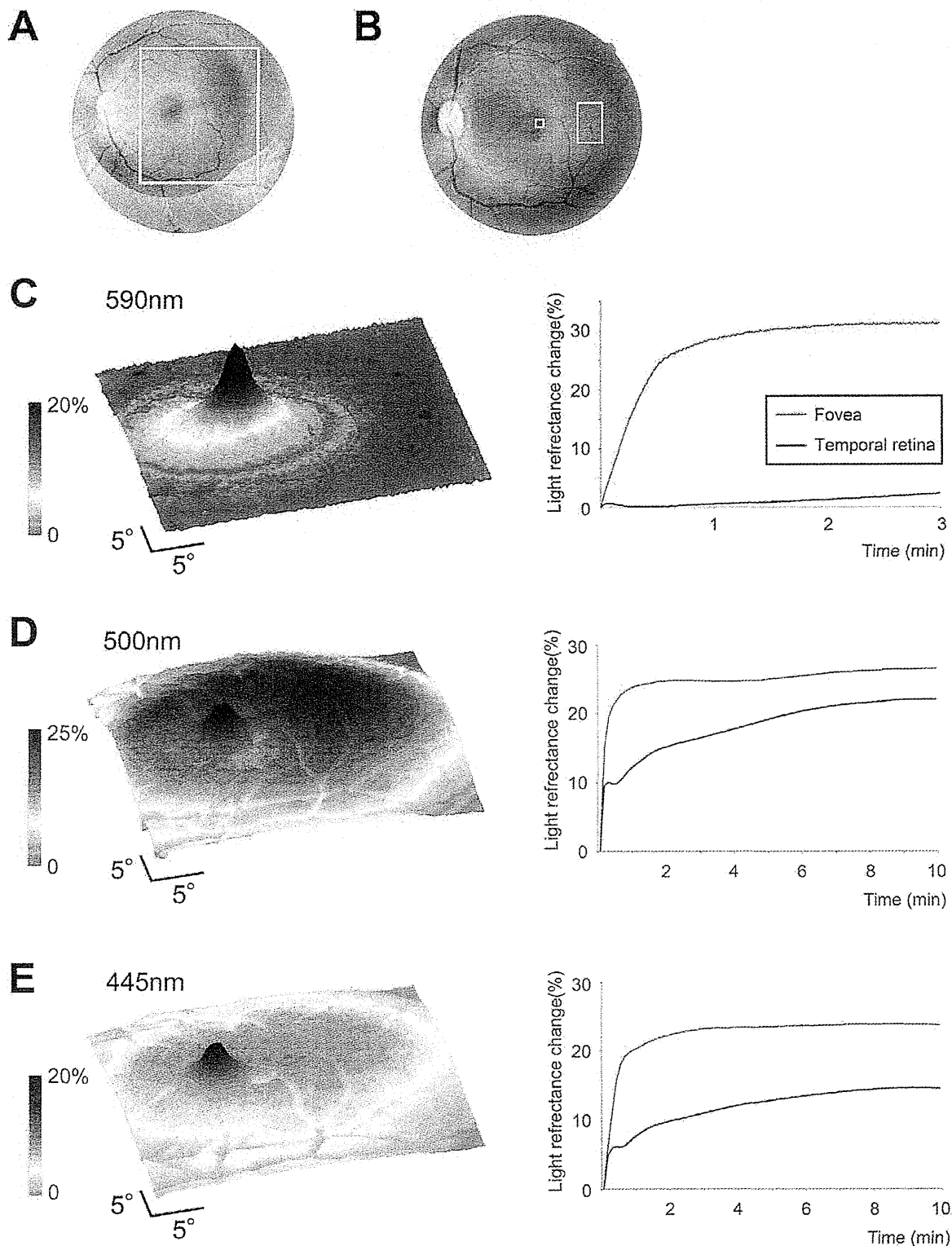
FIGURE 1. Bleach-induced light reflectance changes in retina by different wavelengths of light. (**A, B**) Regions in the macaque retina for the topographic (**A**) and time course analyses (**B**). A small square in **B** indicates the location of the fovea and a rectangle indicates the location of the temporal retina. (**C-E**) Pseudo-colored topographic map of the bleach-induced light reflectance changes (*left*), and time course in the fovea and temporal retina with high intensity light of 5.35 log phot. td for 590 nm (**C**), 6.54 log scot. tld for 500 nm (**D**), and 4.58 log phot. td for 445 nm (*right*) (**E**). Color scales indicate the reflectance changes (%) at the completion of each recording period relative to the reflectance at the beginning. Red lines indicate the time course at the fovea and blue lines for the temporal retina. Data from Monkey 1 are presented.

Rod response
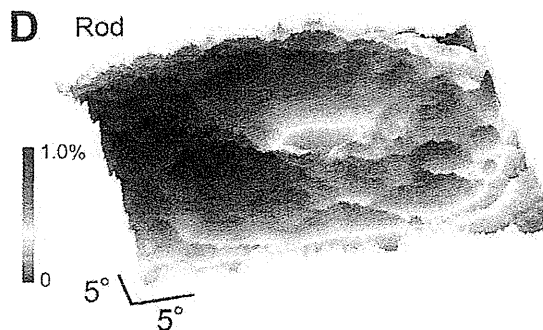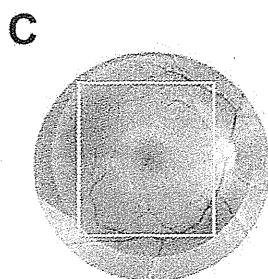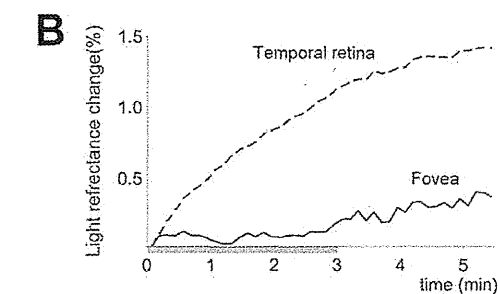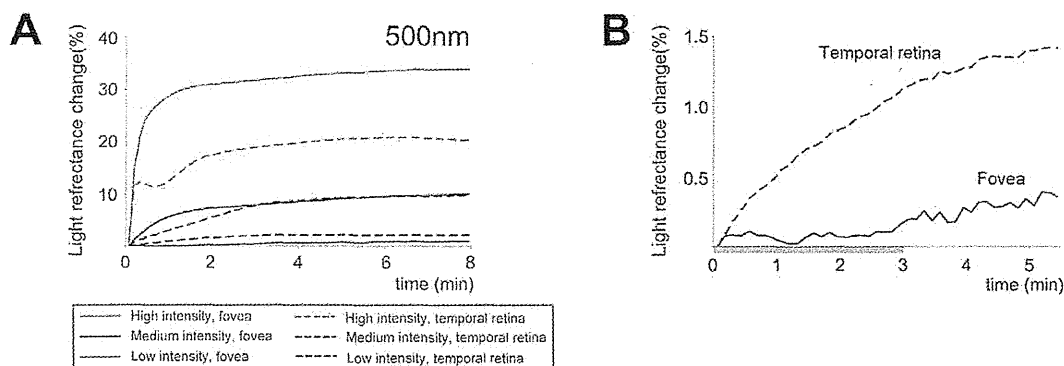
S-cone response
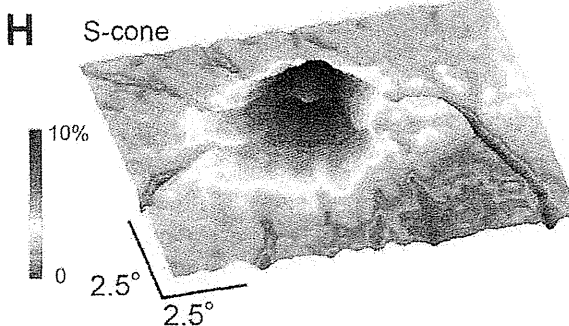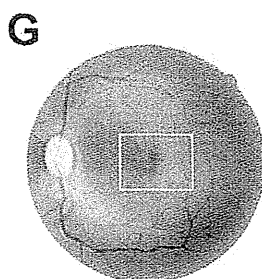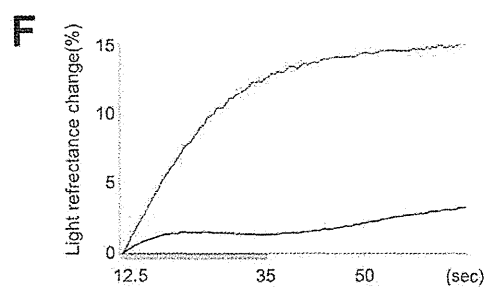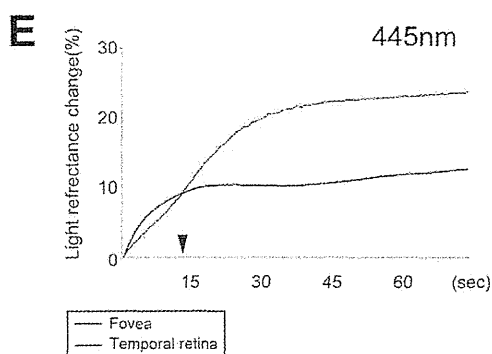
Figure 2. Time-course analyses for the rod (A-D) and S-cone (E-H) responses. (A) Time courses for 500 nm at three different intensities; 6.54 log scot. tld for strong, 5.14 log scot. tld for medium, and 4.73 log scot. tld for weak intensity. Time course at the fovea is represented by solid lines and those at the temporal retina by dotted lines. (B) Expanded image of the time course for the weak 500 nm light (4.73 log scot. tld) for the initial five minutes. The response at the fovea remains flat during the initial three minutes. (C, D) Reflectance topographic map for weak 500 nm light (4.73 log scot. tld) during the initial three minutes (D) measured in the posterior-pole region in (C). The color scale indicates the reflectance changes (%) at 3 minutes. (E, F) Expanded time course for the 455 nm light for the initial 75 seconds (E), and re-plotted reflectance changes relative to the

Retinal Densitometry System and Data Analyses

A modified commercial digital fundus camera system (NM-1000, Nidek, Aichi, Japan) was used to observe and measure continuously the light reflectance changes from the ocular fundus. The fundus images were recorded with a CCD video camera (PX-30BC, Primetech Engineering, Tokyo, Japan), and the images were digitized with an IBM/PC-compatible computer equipped with a video frame grabber board (Corona II, Matrox, Quebec, Canada; gray-level resolution 10 bits, spatial resolution 640 × 480, temporal resolution 1/30 seconds). The optical pathway was modified to illuminate the entire posterior pole region homogeneously for 35 degrees in diameter by inserting a neutral density filter within the optical pathway that was conjugate to the retina. The density of the filter was the highest at the center and decreased gradually toward the periphery to compensate for the highest luminance along the optical axis, which is characteristic to commercial fundus cameras. With this filter, the differences of the estimated retinal luminances within the region of interest were within ± 10%.

Following dark adaptation for one hour, the fundus was illuminated continuously in the dark room with the light from a halogen lamp filtered through one of the three band pass interference filters: blue ($\lambda_{max} = 445 \pm 30$ nm) for S-cone, green ($\lambda_{max} = 500 \pm 15$ nm) for rods, and yellow ($\lambda_{max} = 590 \pm 15$ nm) for M/L-cones. Because the maximum absorption of the M and L cones was close, that is 535 nm for M-cones and 565 nm for L-cones, and differentiation between M- and L-cones in this method was technically difficult, we did not aim to segregate the response topography of these two types of cones. These cones thus were referred to as M/L-cones in this study.

The bleaching of the photopigments was measured as increases in light reflectance from the ocular fundus, that is a brightening. The time course of the reflectance changes was calculated as follows. The gray-scale values of the images obtained after the stimulus were divided, pixel by pixel, by those obtained during a 0.5-second period at the beginning of the trial. This ratio was rescaled to 256 levels of gray-scale resolution to show the stimulus-induced reflectance changes. In each trial, the reflectance was recorded for as long as 11 minutes, which is the maximum recording duration possible in our computer system. Spatial averaging (3 × 3 pixels, i.e. 0.15 × 0.15 degrees, for mapping M/L- and S-cones, or 5 × 5 pixels, i.e. 0.25 × 0.25 degrees, for rods) was performed to build up topographies of retinal responses.

For measuring the rod reflectance changes of the peaks not located in the macular region, six trials were performed consecutively to measure the light reflectance changes in different retinal locations (Fig. 3B). The topographies of these trials were merged to map the responses over 40 degrees in diameter.

We made measurements on three monkeys, and the results with unwanted physiological artifacts, such as the large decrease of reflectance along the vessels due to absorption by hemoglobin and pulsation-induced reflectance changes at the edge of the optic disk, were excluded from the response topographies.

RESULTS

Topography and Time Course of Maximum Bleaching for Each Band Pass Filter

We bleached the retina with different wavelengths of light, and the topographic distribution of the bleaching patterns with yellow (5.35 log phot. td), green (6.54 log scot. tld) and blue (4.58 log phot. td) are shown in Figure 2. The time course of

reflectance changes at the foveal area of 1.75 degrees in diameter and temporal retina 15.0 degrees from the center are shown. The light through the yellow (590 nm) filter bleached the M- and L- cones exclusively,[18,20,34,35] and the changes in the reflectance represented a combination of M/L-cones. The topographic profile showed a high and steep peak of light reflectance increase at the foveal center, which decreased gradually toward the periphery (Fig. 1C).

The green (500 nm) wavelength generally bleaches rods, S-, and M/L-cones,[18,20,34,35] and the topographic changes in reflectance caused by 500 nm light represents the bleaching of all types of photoreceptors. There were high peaks of light reflectance changes at the fovea and the circular region surrounding the macula at an eccentricity of the optic disc (Fig. 1D). The time course of the light reflectance changes was monophasic at the fovea, but biphasic at the temporal retina. The biphasic time course was observed at all retinal locations except for the fovea, and can be explained by the bleaching processes of rod photoreceptors, that is bleaching of 11-cis-retinal to Meta-II intermediates (peak 380 nm) for the initial phase and the bleaching of Meta-III intermediates (peak 465 nm) to all-transretinal and opsin in the late phase.[36,37] These findings indicated that the response topography at the fovea is dominated by bleaching of cones and that in the peripheral region is dominated by bleaching of rods.

Both the S-cones and rods are sensitive to 445 nm,[18,20,34,35] and the topographic changes in the reflectance pattern after bleaching with the green (445 nm) filter represents mainly the bleaching of both rods and S-cones. However, the M/L cones also absorb this wavelength. As with bleaching with 500 nm, the bleaching profile showed that there were peaks of light reflectance changes at the fovea and the circular region surrounding the macula (Fig. 1E). However, the foveal peak was not steep as with 590 or 500 nm but more rounded. This indicated that the reflectance topography at the fovea was not dominated by bleaching of M/L-cones, which should be the maximum at the foveal center. The time course of the light reflectance changes was monophasic at the fovea but biphasic at the temporal retina, as it was with 500 nm. This indicated that the reflectance topography in the peripheral region is dominated by the bleaching of rods.[36,37]

Mapping Rod and S-Cone Responses Based on Bleaching Time Course

The time courses of the reflectance changes during bleaching by 500 nm of different intensities are shown in Figure 2A. With high intensity of 6.54 log scot. tld, the reflectance changes were greater at the fovea (39.9%) than at the temporal retina (20.4%) 8 minutes following the onset of bleaching (Fig. 2A, red line). With low intensity light of 4.73 log scot. tld, the light reflectance changes were lower at the fovea (1.03%) than at the temporal retina (2.28%, Fig. 2A, black line). In addition, during the initial three minutes of bleaching with low intensity light, the foveal response was minimal and remained at 0.1% (Fig. 2B, solid line). This indicated that bleaching of rod photoreceptors could be isolated by measuring the reflectance changes with low light intensity during the initial three minutes. Thus, the topographic distribution of the bleaching of rods could be obtained, and it had a donut-shaped circular

---

reflectance value at 12.5 sec after the onset (*arrowhead* in E) (F). The response at the temporal retina remains almost flat between 12.5 to 35.0 seconds in (F). (G, H) The response topographies for 445 nm at 35.0 seconds shown in (F) and (H) measured in the perimacular region in (G). The color scale indicates the relative reflectance changes (%) at 35.0 minutes to the reflectance at 12.5 minutes. Data from Monkeys 2 and 1 are presented for rod and S-cone, respectively.
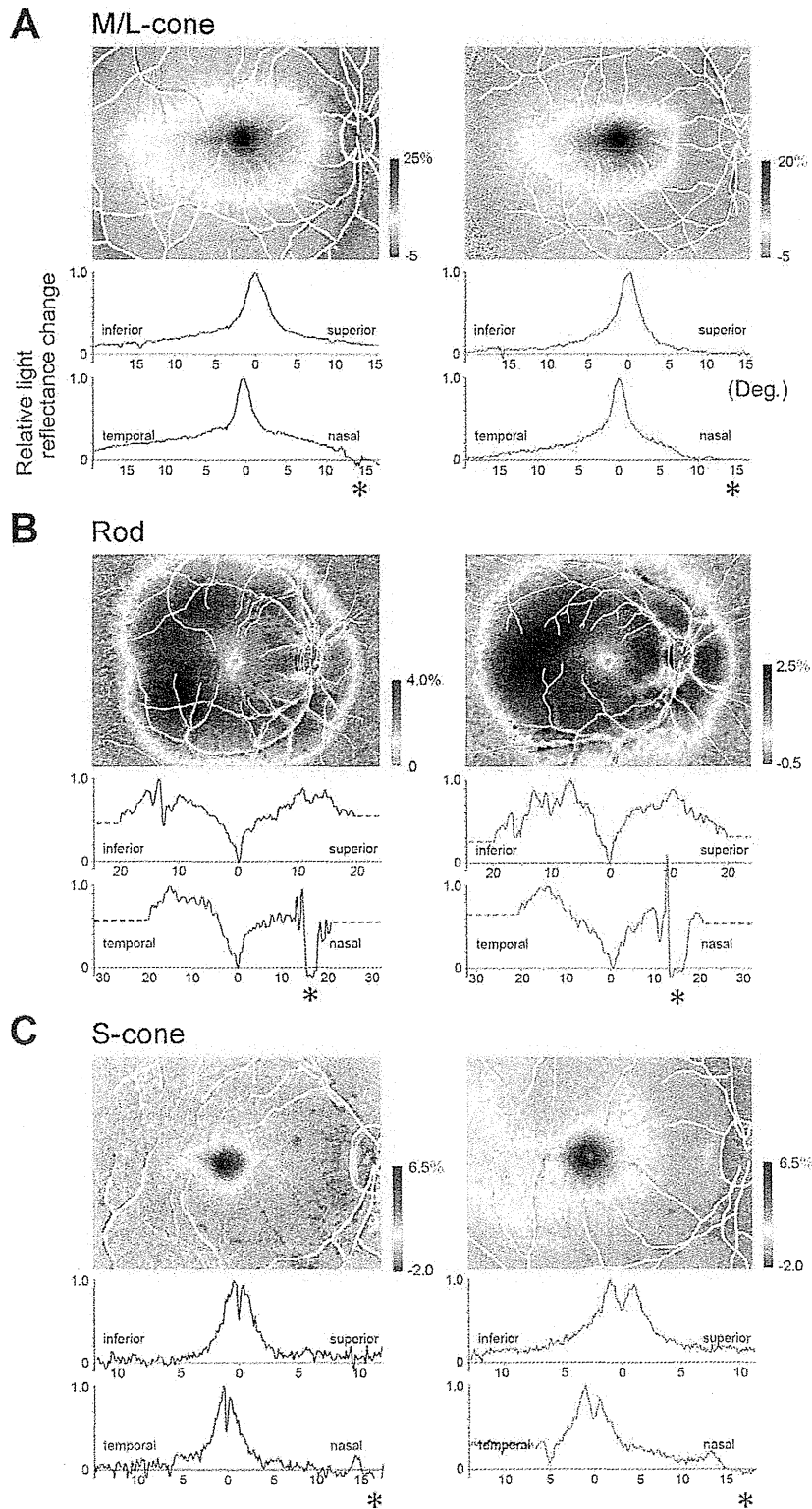
FIGURE 3. Pseudo-color functional topographies for the three types of photoreceptors in two monkeys. (A-C) pseudo-colored functional topographic maps for the three types of photoreceptors (*upper*) and relative response values to the peak (1.0) in the vertical and horizontal profile along the foveal center (*lower*). (A) Response topographies for the M/L cones obtained by 5.35 log phot. td between 60 to 180 seconds following the illumination. (B) Response topographies for the rods obtained by 4.73 log scot. tld between 52.5 to 150 seconds following the illumination. The response profiles outside the region of interest are shown as dotted lines. (C) Response topographies for the S-cone, obtained by 4.58 log phot. td between 30 to 60 seconds following the illumination. Locations of the retinal vessels are overlaid by white lines. Zero degree in the response profile

pattern with an annular peak at an eccentricity of 9.4 to 14.0 degrees from the fovea (Fig. 2D).

The light reflectance changes with 445 nm of 4.58 log phot. td during the initial 75 seconds are expanded in Figure 2E. The time-course at the temporal retina was flatter 12.5 seconds after the onset of bleaching (Fig. 2E, blue line). The reflectance changes relative to the reflectance value at 12.5 seconds after the onset (arrowhead in Fig. 2E) are re-plotted in Figure 2F. During the initial 22.5 seconds (underlined by gray), the degree of reflectance increased to 13.7% at the fovea (red line), but remained flat at the temporal retina (blue line). The light reflectance at the peripheral region did not increase during this period due to the conversion from Meta-II intermediates (peak 380 nm) to Meta-III intermediates (peak 465 nm) of the rod photopigments.[36,37] These changes indicated that the topography obtained during this period did not reflect the responses of rods but was dominated by S-cones. Thus, the topography of S-cone bleaching in the macula could be obtained, and it had a volcano-shaped activation with the foveal center largely excavated (Fig. 2H). This is considered to reflect the reduced number of S-cones at the fovea.

Functional Topography of M/L Cones, Rods, and S-Cones

By considering the preferred wavelengths and the characteristic time courses of the reflectance changes, we have shown the functional topographies of the M/L-cones, rods and S-cones in two monkeys (Fig. 3) in horizontal and vertical sections. The distribution of M/L-cones response had a steep peak at the foveal center and was elongated horizontally. The distribution of rod responses was minimum at the foveal center and maximum along the circular region at the eccentricity of the optic disc. The distribution of S-cone responses was highest at the fovea and was excavated centrally. There was a circular region with the maximal responses at 0.38 to 1.0 degrees from the foveal center.

DISCUSSION

We determined the functional topographic maps of rods, M/L-cones, and S-cones based on the differences in retinal reflectance changes after a selective bleaching of the photopigments by using a flood illumination camera system. A confocal SLO system also could have been used because it has the better spatial resolution. In addition, the intensity of illumination falling on the retina can be homogeneous and modifications of the optical pathway would not be needed as with the fundus camera. However, the most important part of this study was not the imaging resolution alone, but the ability to obtain functional topographic maps of different types of photoreceptors by using different combinations of wavelengths, stimulus intensities, and stimulus durations (Fig. 2). These combinations allowed us to segregate the responses of the different types of photoreceptors. We conducted preliminary experiments with various band pass interference filters and concluded that the combination of 445, 500, and 590 nm filters was ideal for our purposes. In that sense, the simplicity of a flood illumination camera system was advantageous for us.

In the M/L cones (Fig. 3A), the reflectance pattern was approximately equal to that obtained by anatomical studies in macaque and human retinas.[3,4] The reflectance distribution was elongated horizontally with a peak at the foveal center.

In the rods (Fig. 3B), the reflectance changes were minimal at the foveal center, and increased rapidly toward the periphery. The reflectance distribution had a "rod ring" at the eccentricity of the optic disc, that is 9.4 to 14.0 degrees from the center as has been detected by anatomical studies.[3,4] The vertical gradient toward the superior retina described by Curcio et al.[3,4] could not be observed, but instead, the rod responses were maximum at the temporal region along the rod ring.

In the S-cones (Fig. 3C), the reflectance distribution had a volcano-like excavation at the foveal center. The S-cone-free region at the foveal center has been found in macaques and humans anatomically[2,5,7] and psychophysically.[11,13,38] Our results showed that S-cones are functionally minimal at the foveal center in the macaques. The diameter of the ring-shaped peaks with maximal reflectance changes was 0.83 degrees (vertically) x 0.75 degrees (horizontally) in M1 and 1.99 × 1.55 degrees in M2 (Fig. 1C). The eccentricities of the S-cone peaks were within the variations of those obtained by anatomical[2,5,7] and psychophysical studies.[11,13,38] The locations of the peaks of the S-cone responses varied among individuals and the ring-shaped peaks looked vertically elongated. We should note that the reflectance topography of S-cones was shown reliably only in the macular region because the S-cone activities in the periphery were relatively small[12] and were cancelled by the rod-induced light reflectance changes (Fig. 2E and 2F).

There are some discrepancies between the results of earlier anatomical studies and our imaging results. This is because the densitometry technique does not depend solely on the density of photoreceptors, but also on the length of photoreceptor outer segments, that is density of photopigments in each photoreceptor. The goal of our study, however, was not to map the density of the photoreceptors, which has been done already through the series of studies by Curcio et al.,[3–5] but to draw the activity-dependent topography of the photoreceptors, which may confirm and augment the response topography obtained by, for example, mutifocal ERGs.

In our technique of fundus reflectometry, the optical pathway was adjusted to illuminate the posterior retina homogeneously so that the results reflected the relative reflectance distribution more accurately. However, there are some possible artifacts by which the reflectance changes may be either over- or underestimated in particular regions. First, the presence of scattered light from the inner limiting membrane and nerve fiber layer around the macula may cause an underestimation of the bleach-induced light reflectance changes.[31] A quantitative evaluation of this scattering effect was very difficult to obtain because the topographies we had presented did not seem to be affected by such artifacts in the peri-macular regions (Fig. 3A).

Second, the effect of intrinsic optical signals, which reflect the hemoglobin-induced light reflectance changes following neural activation, must be considered.[39,40] The intrinsic signals also would be observed in the retina as stimulus-induced light reflectance decreases.[41–43] The intrinsic signals are prominent at a wavelength with the maximum hemoglobin absorption (540-580 nm), and in our response topographies, regions corresponding to the optic disc and large retinal vessels, which are rich in red blood cells, might have had relatively smaller reflectance increases due to the intrinsic signals (Figs. 1 and 3). The maximal light reflectance decrease due to intrinsic signals

indicates the location of fovea. The location of the optic disk is indicated by an asterisk. Data from Monkeys 1 and 3 for M/L cone, Monkeys 2 and 3 for rods, and Monkeys 1 and 2 for S-cones are presented.

in our recording protocol, however was estimated to be 1.0% to 2.0% at the optic disc, where intrinsic signals could be solely and maximally observed.[42] Thus, the intrinsic signals probably had little effect on the overall bleaching topographies.

Third, the Stiles-Crawford effect,[44] the directional sensitivity of the cone photoreceptors, may change the reflectance intensities depending on the position of the illumination center over the retina. In the horizontal response profiles of S-cones (Fig. 3C), the circular peak response was slightly higher in the temporal fovea than in the nasal fovea. This was considered to reflect the Stiles-Crawford effect because the illumination was centered 2.56 degrees temporal to the foveal center, and the rays of light passed cone photoreceptors less oblique at the temporal fovea than at the nasal fovea.

The bleach-induced reflectance changes are affected by such artifacts and may not reflect the distribution of photoreceptor activities accurately.

A clinical application of this technique may not be easy because subjects must keep staring at the fixation target with very bright background illumination for relatively long times. However, there are recent reports using SLO[31,45,46] or a snapshot imaging system[33] to measure cone- or rod-induced response topography. Unfortunately, the response distribution of rods or S-cone responses cannot be extracted accurately as in this study. Our results will provide us with valuable photoreceptor activities in macaque retinas, which can complement those obtained either anatomically[2-5,7] or psychophysically.[10-15,38]

References

1. Osterberg G. Topography of the layer of rods and cones in the human retina. *Acta Ophthalmol.* 1935;13:6–97.

2. de Monasterio FM, McCrane EP, Newlander JK, Schein SJ. Density profile of blue-sensitive cones along the horizontal meridian of macaque retina. *Invest Ophthalmol Vis Sci.* 1985; 26:289–302.

3. Packer O, Hendrickson AE, Curcio CA. Photoreceptor topography of the retina in the adult pigtail macaque (Macaca nemestrina). *J Comp Neurol.* 1989;288:165–183.

4. Curcio CA, Sloan KR, Kalina RE, Hendrickson AE. Human photoreceptor topography. *J Comp Neurol.* 1990;292:497–523.

5. Curcio CA, Allen KA, Sloan KR, et al. Distribution and morphology of human cone photoreceptors stained with anti-blue opsin. *J Comp Neurol.* 1991;312:610–624.

6. Mollon JD, Bowmaker JK. The spatial arrangement of cones in the primate fovea. *Nature.* 1992;360:677–679.

7. Bumsted K, Hendrickson A. Distribution and development of short-wavelength cones differ between Macaca monkey and human fovea. *J Comp Neurol.* 1999;403:502–516.

8. Andrade da Costa BL, Hokoc JN. Photoreceptor topography of the retina in the New World monkey Cebus apella. *Vision Res.* 2000;40:2395–2409.

9. Cornish EE, Hendrickson AE, Provis JM. Distribution of short-wavelength-sensitive cones in human fetal and postnatal retina: early development of spatial order and density profiles. *Vision Res.* 2004;44:2019–2026.

10. Wald G. The receptors of human color vision. *Science.* 1964; 145:1007–1016.

11. Wald G. Blue-blindness in the normal fovea. *J Opt Soc Am.* 1967;57:1289–1301.

12. Wooten BR, Wald G. Color-vision mechanisms in the peripheral retinas of normal and dichromatic observers. *J Gen Physiol.* 1973;61:125–145.

13. Castaño JA, Sperling HG. Sensitivity of the blue-sensitive cones across the central retina. *Vision Res.* 1982;22:661–673.

14. Birch DG, Herman WK, deFaller JM, Disbrow DT, Birch EE. The relationship between rod perimetric thresholds and full-field rod ERGs in retinitis pigmentosa. *Invest Ophthalmol Vis Sci.* 1987;28:954–965.

15. Pulos E. Changes in rod sensitivity through adulthood. *Invest Ophthalmol Vis Sci.* 1989;30:1738–1742.

16. Rushton WA. The rhodopsin density in the human rods. *J Physiol.* 1956;134:30–46.

17. Hood C, Rushton WA. The Florida retinal densitometer. *J Physiol.* 1971;217:213–229.

18. Brown PK, Wald G. Visual pigments in human and monkey retinas. *Nature.* 1963;200:37–43.

19. Rushton WA. Cone pigment kinetics in the protanope. *J Physiol.* 1963;168:374–388.

20. Brown PK, Wald G. Visual pigments in single rods and cones of the human retina. direct measurements reveal mechanisms of human night and color vision. *Science.* 1964;144:45–52.

21. Alpern M, Maaseidvaag F, Oba N. The kinetics of cone visual pigments in man. *Vision Res.* 19771;11:539–549.

22. Alpern M. Rhodopsin kinetics in the human eye. *J Physiol.* 1971;217:447–471.

23. Mizuno K, Majima A, Ozawa K, Ito H. Red-free light fundus photography. Photographic optogram. *Invest Ophthalmol.* 1968;7:241–249.

24. Highman VN, Weale RA. Rhodopsin density and visual threshold in retinitis pigmentosa. *Am J Ophthalmol.* 1973; 75:822–832.

25. Sheorey UB. Clinical assessment of rhodopsin in the eye. Using a standard fundus camera and a photographic technique. *Br J Ophthalmol.* 1976;60:135–141.

26. Kilbride PE, Read JS, Fishman GA, Fishman M. Determination of human cone pigment density difference spectra in spatially resolved regions of the fovea. *Vision Res.* 1983;23:1341–1350.

27. Kilbride PE, Keehan KM. Visual pigments in the human macula assessed by imaging fundus reflectometry. *Appl Opt.* 1990;29: 1427–1435.

28. Faulkner DJ, Kemp CM. Human rhodopsin measurement using a T.V.-based imaging fundus reflectometer. *Vision Res.* 1984; 24:221–231.

29. Kemp CM, Faulkner DJ, Jacobson SG. The distribution and kinetics of visual pigments in the cat retina. *Invest Ophthalmol Vis Sci.* 1988;29:1056–1065.

30. van Norren D, van de Kraats J. Imaging retinal densitometry with a confocal Scanning Laser Ophthalmoscope. *Vision Res.* 1989;29:1825–1830.

31. Elsner AE, Burns SA, Hughes GW, Webb RH. Reflectometry with a scanning laser ophthalmoscope. *Appl Opt.* 1992;31: 3697–3710.

32. Berendschot TT, DeLint PJ, van Norren D. Fundus reflectance-historical and present ideas. *Prog Retin Eye Res.* 2003;22:171–200.

33. Kazato Y, Shibata N, Hanazono G, Suzuki W, Tanifuji M, Tsunoda K. Novel snapshot imaging of photoreceptor bleaching in macaque and human retinas. *Jpn J Ophthalmol.* 2010;54:349–356.

34. Bowmaker JK, Dartnall HJ. Visual pigments of rods and cones in a human retina. *J Physiol.* 1980;298:501–511.

35. Bowmaker JK, Dartnall HJ, Mollon JD. Microspectrophotometric demonstration of four classes of photoreceptor in an old world primate, Macaca fascicularis. *J Physiol.* 1980;298:131–143.

36. Imai H, Kuwayama S, Onishi A, Morizumi T, Chisaka O, Shichida Y. Molecular properties of rod and cone visual pigments from purified chicken cone pigments to mouse rhodopsin in situ. *Photochem Photobiol Sci.* 2005;4:667–674.

37. Shichida Y, Imai H, Imamoto Y, Fukada Y, Yoshizawa T. Is chicken green-sensitive cone visual pigment a rhodopsin-like pigment - a comparative-study of the molecular-properties between chicken green and rhodopsin. *Biochemistry.* 1994; 33:9040–9044.

38. Williams DR, MacLeod DI, Hayhoe MM. Punctate sensitivity of the blue-sensitive mechanism. *Vision Res.* 1981;21:1357–1375.

39. Grinvald A, Lieke E, Frostig RD, Gilbert CD, Wiesel TN. Functional architecture of cortex revealed by optical imaging of intrinsic signals. *Nature.* 1986;324:361–364.

40. Bonhoeffer T, Grinvald A. Optical imaging based on intrinsic singals: the methodology. In: Toga AW, Mazziotta JC, eds. *Brain Mapping.* San Diego: Academic Press; 1996:55–97.

41. Tsunoda K, Oguchi Y, Hanazono G, Tanifuji M. Mapping cone- and rod-induced retinal responsiveness in macaque retina by optical imaging. *Invest Ophthalmol Vis Sci.* 2004;45:3820–3826.

42. Hanazono G, Tsunoda K, Kazato Y, Tsubota K, Tanifuji M. Evaluating neural activity of retinal ganglion cells by flash-evoked intrinsic signal imaging in macaque retina. *Invest Ophthalmol Vis Sci.* 2008;49:4655–4663.

43. Tsunoda K, Hanazono G, Inomata K, Kazato Y, Suzuki W, Tanifuji M. Origins of retinal intrinsic signals: a series of experiments on retinas of macaque monkeys. *Jpn J Ophthalmol.* 2009;53:297–314.

44. Stiles WS, Crawford BH. The luminous efficiency of rays entering the eye pupil at different points. *Proc Roy Soc London Series B-Containing Papers of a Biological Character.* 1933;112:428–450.

45. Elsner AE, Burns SA, Beausencourt E, Weiter JJ. Foveal cone photopigment distribution: small alterations associated with macular pigment distribution. *Invest Ophthalmol Vis Sci.* 1998;39:2394–2404.

46. Sekiryu T, Iida T, Maruko I, Horiguchi M. Clinical application of autofluorescence densitometry with a scanning laser ophthalmoscope. *Invest Ophthalmol Vis Sci.* 2009;50:2994–3002.

A Longitudinal Study of Stargardt Disease: Clinical and Electrophysiologic Assessment, Progression, and Genotype Correlations

KAORU FUJINAMI, NOEMI LOIS, ALICE E. DAVIDSON, DONNA S. MACKAY, CHRIS R. HOGG, EDWIN M. STONE, KAZUSHIGE TSUNODA, KAZUO TSUBOTA, CATEY BUNCE, ANTHONY G. ROBSON, ANTHONY T. MOORE, ANDREW R. WEBSTER, GRAHAM E. HOLDER, AND MICHEL MICHAELIDES

• PURPOSE: To investigate the clinical and electrophysiologic natural history of Stargardt disease and correlate with the genotype.

• DESIGN: Cohort study of 59 patients.

• METHODS: Clinical history, examination, and electrophysiologic assessment were undertaken in a longitudinal survey. Patients were classified into 3 groups based on electrophysiologic findings, as previously published: Group 1 had dysfunction confined to the macula; Group 2 had macular and generalized cone system dysfunction; and Group 3 had macular and both generalized cone and rod system dysfunction. At baseline, there were 27 patients in Group 1, 17 in Group 2, and 15 in Group 3. Amplitude reduction of > 50% in the relevant electroretinogram (ERG) component or a peak time shift of > 3 ms for the 30 Hz flicker ERG or bright flash a-wave was considered clinically significant ERG deterioration. Molecular screening of ABCA4 was undertaken.

• RESULTS: The mean age at baseline was 31.7 years, with the mean follow-up interval being 10.5 years. A total of 22% of patients from Group 1 showed ERG group transition during follow-up, with 11% progressing to Group 2 and 11% to Group 3. Forty-seven percent of patients in Group 2 progressed to Group 3. There was clinically significant ERG deterioration in 54% of all subjects: 22% of Group 1, 65% of Group 2, and 100% of Group 3. At least 1 disease-causing ABCA4 variant was identified in 47 patients.

• CONCLUSIONS: All patients with initial rod ERG involvement demonstrated clinically significant electrophysiologic deterioration; only 20% of patients with normal full-field ERGs at baseline showed clinically significant progression. Such data assist counseling by providing more accurate prognostic information and are also highly relevant in the design, patient selection, and monitoring of potential therapeutic interventions. (Am J Ophthalmol 2013;█:█–█. © 2013 by Elsevier Inc. All rights reserved.)

S TARGARDT DISEASE IS ONE OF THE MOST COMMON inherited retinal disorders, with a prevalence of 1 in 10 000. It is inherited as an autosomal recessive trait.[1–3] Most cases present with central visual loss and there is typically macular atrophy with yellow-white flecks at the posterior pole, which are at the level of the retinal pigment epithelium (RPE). Autofluorescence (AF) imaging and fluorescein angiography can be helpful in confirming the diagnosis.[4–8] The age of onset is usually in the early teens, but there is wide variation, with a later age of onset being associated with a better visual prognosis.[7,9]

Since the discovery of ABCA4 variants underlying Stargardt disease, multiple studies have described the wide phenotypic variability in ABCA4-associated retinopathy.[9–19] There is also extensive allelic heterogeneity, with more than 600 sequence variations having been reported to date in the ABCA4 gene.[10,13,20–30] These 2 features make comprehensive genotype/phenotype correlations challenging. A previous cross-sectional study of 63 patients with Stargardt disease classified subjects into 3 functional electroretinogram (ERG) phenotypes: Group 1: dysfunction confined to the macula; Group 2: macular and generalized cone ERG abnormalities; and Group 3: macular and both generalized cone and rod ERG abnormalities.[31] Differences in rod or cone function between groups could not be explained by differences in age of onset or duration of disease. It was thereby concluded that these 3 groups may represent distinct phenotypic subtypes of Stargardt disease and it was suggested, based on the cross-sectional data, that patients in Group 1 were likely to have a more favorable prognosis.

The purpose of the present study was to determine whether longitudinal data from a cohort of Stargardt disease patients support the value of full-field ERG to visual prognosis previously suggested by cross-sectional data. We have assessed the progression of Stargardt disease by repeated clinical and electrophysiologic examinations over time and probed whether the initial phenotype predicts long-term prognosis.

PATIENTS AND METHODS

A COHORT OF 59 PATIENTS WITH A CLINICAL DIAGNOSIS OF Stargardt disease and a minimum of 7 years of follow-up were ascertained at Moorfields Eye Hospital. All patients were first diagnosed between 1997 and 2000, with the latest examinations performed between 2009 and 2011. The baseline clinical and electrophysiologic characteristics of 33 of these 59 patients have been previously reported.[31] The panel included 5 sibships (4 sibling pairs and 1 set of 3 siblings). Informed consent was obtained from all participants. Blood samples were taken from all individuals for DNA extraction. The protocol of the study adhered to the tenets of the Declaration of Helsinki and was approved by the Ethics Committee of Moorfields Eye Hospital.

- CLINICAL ASSESSMENT: Fifty-nine patients were assessed on at least 2 occasions, with the first and most recent visits taken as the baseline and "follow-up" examinations, respectively, for the purposes of data analysis. A full medical history was obtained and a comprehensive ophthalmologic examination performed for all patients. The age of onset was defined as the age at which visual loss was first noted by the patient. The duration of the disease was calculated as the difference between age at onset and age at the baseline examination when an electrophysiologic assessment was obtained. The interval of observation was determined by the difference between the age at baseline and the age at the most recent electrophysiologic examination. Clinical assessment included best-corrected Snellen visual acuity (converted to equivalent logarithm of minimal angle of resolution [logMAR] visual acuity for the purpose of data analysis), dilated ophthalmoscopy, and color fundus photography.

- ELECTROPHYSIOLOGY: All patients underwent electrophysiologic assessment, to include full-field ERG and pattern electroretinography (PERG), incorporating the minimum standards of the International Society for Clinical Electrophysiology of Vision (ISCEV).[32,33] ERG examination was comprehensive and included: (1) dark-adapted dim flash 0.01 candela second $(cd \cdot s)/m^2$ (dark-adapted 0.01); (2) dark-adapted bright flash 11.0 $cd \cdot s/m^2$ (dark-adapted 11.0); (3) light-adapted 3.0 $cd \cdot s/m^2$ 30 Hz flicker ERG (light-adapted 30 Hz); and (4) light-adapted 3.0 $cd \cdot s/m^2$ at 2 Hz (light-adapted 3.0). All recordings were performed with gold-foil recording electrodes with reference electrodes at the ipsilateral outer canthi.

The patient data were compared against those of 16 healthy subjects younger than 50 years and 19 subjects older than 50 years, to maintain consistency with the original cross-sectional study.[4,31,34] PERGs were compared against those from 28 normal subjects, with N95 peak time not being used for interpretation because of its accepted variability.[35] The limits of ERG normality were defined for all the components of the ERG and PERG as the mean value ±2 standard deviations (Supplemental Tables 1 and 2, available at AJO.com). The threshold values for the minimum amplitude/maximum peak time for subjects younger than 50 years were defined as 135 μV/107 ms (dark-adapted 0.01), 250 μV/13 ms and 320 μV/56 ms (dark-adapted 11.0 a- and b-wave, respectively), 70 μV/27 ms (light-adapted 30 Hz), and 30 μV/15 ms and 95 μV/32 ms (light-adapted 3.0 a- and b-wave, respectively); and for patients older than 50 years as 30 μV/117 ms (dark-adapted 0.01), 105 μV/16 ms and 235 μV/57 ms (dark-adapted 11.0 a- and b-wave, respectively), 50 μV/29 ms (light-adapted 30 Hz); and 15 μV/16 ms and 90 μV/32 ms (light-adapted 3.0 a- and b-wave, respectively). The threshold values for the PERG P50 minimum amplitude/maximum peak time were defined as 2.1 μV/58.5 ms.

All the components of the ERG and PERG from each eye were taken into account when classifying patients into 1 of the 3 ERG groups at baseline and follow-up. Group 1 was defined as PERG abnormality with normal ERGs. In Group 2, there was PERG abnormality and abnormal cone function (assessed with light-adapted 30 Hz and light-adapted 3.0) on ERG. In Group 3, there was additional rod ERG abnormality (assessed using dark-adapted 0.01 and dark-adapted 11.0). The overall classification was based on the more severe eye in the small number of patients with different ERG groups between eyes. The data obtained at follow-up were compared with those at baseline. Concordance for ERG group between siblings was defined as siblings having the same ERG group classification both at baseline and at follow-up.

Amplitude reduction was calculated as the difference between amplitude at baseline and at follow-up. The percentage reduction in amplitudes was obtained by dividing the amplitude reduction by baseline amplitude. A yearly amplitude reduction and a yearly percentage reduction were calculated by dividing the amplitude reduction or the percentage reduction by the follow-up time. A yearly peak time shift (difference between peak time at baseline and at follow-up) was also calculated by dividing by the follow-up time.

An amplitude reduction of over 50% in any ERG component and/or a peak time shift of over 3 ms for the light-adapted 30 Hz ERG or dark-adapted 11.0 ERG a-wave were considered evidence of clinically significant ERG deterioration/progression. Patients were thereby

classified into 2 subsets: those with clinically significant ERG deterioration and those without significant ERG deterioration (stable ERG).

● MUTATION SCREENING: Mutation analysis was performed using the single-stranded conformation polymorphism (SSCP) strategy of the whole coding region of ABCA4 in 33 subjects[36] and the arrayed primer extension (APEX) microarray (ABCR400 chip; Asper Ophthalmics, Tartu, Estonia) for previously reported variants in 27 patients.[23] Direct Sanger sequencing was done in siblings of probands and parents, when available, to confirm segregation of alleles, as well as in 8 subjects either to confirm putative novel variants or where the variants found with SSCP and APEX differed (Supplemental Table 3, available at AJO.com).

Non-null variants were analyzed using 2 software prediction programs: SIFT (Sorting Intolerant from Tolerant; http://sift.jcvi.org/)[37] and PolyPhen2 (http://genetics.bwh.harvard.edu/pph/index.html).[38] All variants were also analyzed for their effect on splicing using the Human Splicing Finder program, version 2.4.1 (http://www.umd.be/HSF/). All variants were compared with variants in the Exome Variant Server, NHLBI Exome Sequencing Project, Seattle, Washington, USA (http://snp.gs.washington.edu/EVS/).

Each patient was classified into 4 mutually exclusive genotype groups on the basis of the molecular analysis: (A) patients with at least 1 null variant, (B) subjects with 2 or more non-null variants, (C) individuals with 1 non-null variant, and (D) patients with no detectable variants. Null variants were those that would be expected to affect splicing, or to introduce a premature truncating codon in the protein if translated. The term "variants" for the purpose of this study includes those sequence changes previously shown to be enriched in Stargardt patients from prior studies, or for very rare variants, those not found at an allele frequency greater than 0.1% on the exome variant database (Accessed March 1, 2012).

● STATISTICAL ANALYSIS: Statistical analysis has been undertaken using data from only 1 eye in each subject. For the 57 patients with the same ERG grouping in both eyes, the eye used for analysis was selected according to the Random Integer Generator (http://www.random.org/). For the 2 patients (Patients 26 and 48) with a different ERG group in each eye, the eye with the more severe ERG grouping (ie, more generalized retinal dysfunction) was selected for analysis.

The Mann-Whitney U test was used to explore whether differences observed between patients with clinically significant electrophysiologic deterioration and those without were statistically significant with regard to age of onset, duration of disease, age at baseline, the interval of observation, logMAR visual acuity at baseline, logMAR visual acuity reduction (defined as the difference between visual acuity

at baseline and at follow-up), and yearly percentage amplitude reduction and yearly peak time shift in both the light-adapted 11.0 a-wave and light-adapted 30 Hz.

The Kruskal-Wallis test with Steel-Dwass multiple comparisons was performed to compare the 3 baseline ERG groups (ERG Group 1, 2, and 3) and the 3 genotype groups (genotype A, B, and C) for the 10 aforementioned parameters. Where evidence was found of a difference between these groups, all pairwise comparisons were made.

The association between genotype group classification and baseline ERG group classification was tested using the Goodman-Kruskal gamma, a measure of association for ordered categories ranging between −1 and +1 for perfect negative or positive association, respectively. P values less than .05 were considered to indicate statistical significance.

All analyses were conducted using MedCalc statistical software version 9.2.1.0 (MedCalc Software, Ostend, Belgium) and Excel Tokei 2010 (Social Survey Research Information Co Ltd, Tokyo, Japan).

RESULTS

● CLINICAL FINDINGS: Fifty-nine patients, 31 female (52%, 31/59) and 28 male (48%, 28/59), were included in the study. All complained of central visual loss with a median age of onset of 20.8 years (range, 5-48 years) and a median duration of disease of 10.9 years (range, 0-31 years). The median ages at baseline and at follow-up were 31.7 and 42.2 years (range, 8-64 and 20-73 years), respectively. The mean follow-up interval was 10.5 years (range, 7-13 years). Seven patients (12%, 7/59) presented before 16 years of age and 52 (88%, 52/59) presented after age 16 years. The median logMAR visual acuities (VA) at baseline and at follow-up were 0.93 (range, 0.0-2.0) and 1.22 (range, 0.0-3.0), respectively, with a median logMAR VA reduction during the follow-up interval of 0.29 (range, −0.78-2.0). The clinical findings are summarized in Table 1 and the eye selected for data analysis is shown in Supplemental Table 3 (available at AJO.com).

At baseline, there were 27 patients (46%, 27/59) in Group 1, 17 (29%, 17/59) in Group 2, and 15 (25%, 15/59) in Group 3, compared at follow-up to 21 patients (36%, 21/59) in Group 1, 12 (20%, 12/59) in Group 2, and 26 (44%, 26/59) in Group 3 (Table 2). The median age of onset for each baseline ERG group was 24.9 years in Group 1, 20.4 years in Group 2, and 14.0 years in Group 3. The median age (years) at examination/logMAR visual acuity at baseline and follow-up for each baseline ERG group was 34.4/0.78 and 45.0/1.00, respectively, in Group 1; 29.6/1.00 and 39.4/1.00, respectively, in Group 2; and 29.1/1.25 and 40.3/1.30, respectively, in Group 3 (Table 3).

Color fundus photographs of eyes in 3 representative cases (Patients 17, 42, and 53) are shown in Figure 1; their

TABLE 1. Clinical Data and Molecular Genetic Status of 59 Patients With Stargardt Disease

Pt	Onset (y)	Age (y)		logMAR VA		Variants Identified[a]
		BL	FU	BL	FU	
1	16	17	26	0.0/1.0	0.0/0.48	c.768G>T / p.Gly863Ala / p.Arg943Gln
2	15	17	25	0.78/0.78	1.0/1.0	p. Arg1443His
3	11	18	27	0.78/1.0	1.0/1.0	**p.Trp439*** / p.Gly863Ala / p.Leu1970Phe
4	19	21	32	0.78/0.78	1.0/1.0	p.Leu2027Phe
5	10	22	30	0.48/0.48	1.0/0.78	p.Gly863Ala / p.Arg943Gln / c.5461-10 T>C
6	18	26	37	0.78/1.0	1.0/1.0	p.Pro1380Phe
7	25	28	40	0.78/1.0	1.3/0.78	ND
8	24	29	38	1.0/0.78	1.0/1.0	p.Phe418Ser / p.Leu2027Phe
9	24	31	44	1.0/1.0	1.3/1.0	c.4253+5 G>T / **p.Gly1507Arg**
10	26	32	44	0.78/0.78	1.0/1.0	p.Cys1490Tyr / p.Arg2030Gln
11	31	34	46	0.18/0.3	0.6/0.7	ND
12	17	35	47	1.0/1.0	1.0/1.0	p.Asn96His
13	23	35	45	1.0/0.3	1.0/0.48	p.Gly1513Profs*1554
14	33	37	48	0.18/1.48	1.0/1.3	ND
15	38	40	51	0.18/0.78	1.0/1.0	p.Arg2107His
16	42	43	53	0.0/0.0	1.0/1.0	ND
17	22	48	59	1.0/1.0	1.0/1.0	p.Cys54Tyr
18	20	49	59	1.0/0.6	1.0/1.0	p.Pro1380Leu / p.Gly1961Glu
19	35	50	61	1.0/0.3	1.0/1.0	p.Arg1108Cys
20	25	56	67	1.3/0.18	1.0/1.0	**p.Trp439*** / p.Gly863Ala
21	48	59	71	1.0/0.78	1.0/1.0	p. Ile156 Val / **p. Cys1455Arg** / p. Phe1839Ser
22	21	22	31	0.3/1.0	1.0/1.0	p.Arg2107His
23	21	23	33	1.0/1.0	1.0/1.0	p.Gly863Ala
24	48	64	73	0.0/1.0	0.18/3.0	p.Tyr1652*
25	17	19	29	0.78/0.3	1.0/1.0	c.5461-10 T>C
26	17	21	33	1.0/0.78	1.0/1.0	ND
27	27	53	66	1.78/1.78	1.3/1.0	p.Ser1071Cysfs*1084
28	5	14	21	0.78/0.78	1.0/1.0	p.Arg408* / **p.Val675Ile**
29	9	15	27	1.08/1.08	1.0/1.0	p.Cys2150Tyr
30	14	24	32	1.0/0.78	1.0/1.0	ND
31	18	28	39	1.0/1.0	1.0/1.0	p.Gly863Ala / p.Arg1108Cys / p.Arg943Gln
32	14	29	37	1.0/1.0	1.0/1.0	p.Arg653Cys / p.Arg2030Gln
33	19	29	40	1.0/1.0	1.0/1.08	ND
34	34	40	49	0.3/0.48	1.0/1.0	p.Gly863Ala / p.Glu1087Lys
35	25	43	54	1.0/1.0	1.0/1.0	p.Cys54Tyr / p.Gly863Ala
36	38	60	69	1.0/1.0	1.3/1.08	p.Val931Met / c.5461-10 T>C
37	10	11	20	1.0/0.78	1.3/1.3	p.Pro1380Leu
38	10	15	23	1.0/1.0	1.3/1.3	p.Ser1071Cysfs*1084 / p.Pro1380Leu
39	24	25	38	1.56/0.3	2.0/2.0	c.5461-10 T>C / c.5714+5 G>A
40	18	26	36	1.3/1.3	2.0/1.3	ND
41	32	33	45	0.48/0.48	1.0/1.0	ND
42	32	35	46	1.3/0.0	3.0/1.0	p.Cys54Tyr
43	30	35	45	0.48/0.48	2.0/1.3	ND
44	15	41	49	1.3/1.3	2.0/1.3	p.Asn965Ser
45	8	8	20	0.78/0.78	1.0/1.0	p.Thr1019Met
46	10	11	23	1.0/1.0	1.0/1.0	p.Thr1019Met
47	8	12	24	2.0/1.56	1.78/1.48	p.Cys2150Tyr
48	17	18	26	1.0/0.78	1.3/1.0	c.5461-10 T>C / p.Leu2027Phe
49	8	21	33	1.3/1.3	2.0/2.0	p.Asp574Aspfs*582
50	8	27	39	2.0/1.56	1.78/1.48	c.5461-10 T>C
51	24	31	43	1.18/1.18	1.08/1.3	p.Arg1640Trp / p.Leu2027Phe